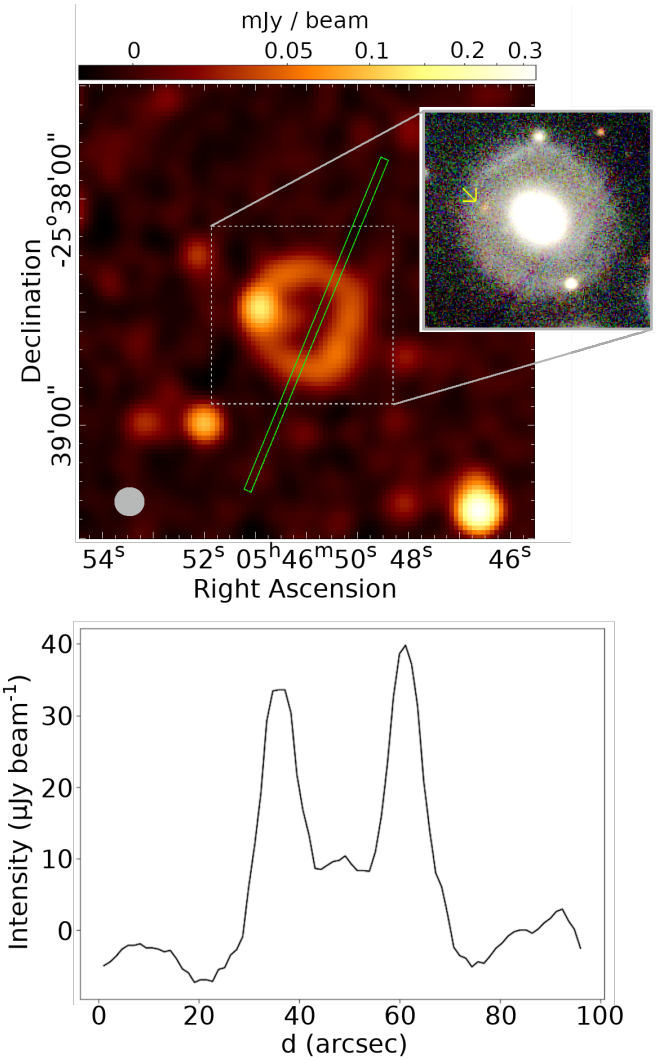

Fig. 25. A ring-like source in Abell 548. *Top*: 7.5″ resolution MGCLS Stokes-*I* intensity image of the ring-like source in the Abell 548 field, centred at RA = $05^{h}46^{m}50.0^{s}$, Dec = −25°38′30.4″. The inset shows the Pan-STARRS *gri*-composite image. The ring hotspot is coincident with a background galaxy, indicated by the yellow arrow. *Bottom*: profile through the centre of the radio ring (green region in the top panel, with the profile starting from the northern end), showing that the structure is filled.

having a spectral index of approximately −1. Such steep, non-thermal spectra are more typical of Sb and later type galaxies (Puxley et al. 1988). A slice through the centre of the ring, shown in the bottom panel of Fig. 25, indicates that there is also emission in the interior of the ring, although there is no central peak typically associated with star-forming spiral galaxies. If the ring is due to star formation, it may have been triggered by interaction with the companion galaxy (z = 0.04648) that lies 75.5″ to the north-east, outside of the region shown in Fig. 25.

8.2. Population studies in Abell 209

Galaxy clusters are populated by two broad classes of galaxies: red elliptical galaxies in which star formation has been quenched, and blue spiral galaxies with ongoing star formation (e.g. Baldry et al. 2004; Taylor et al. 2015; Haines et al. 2017).

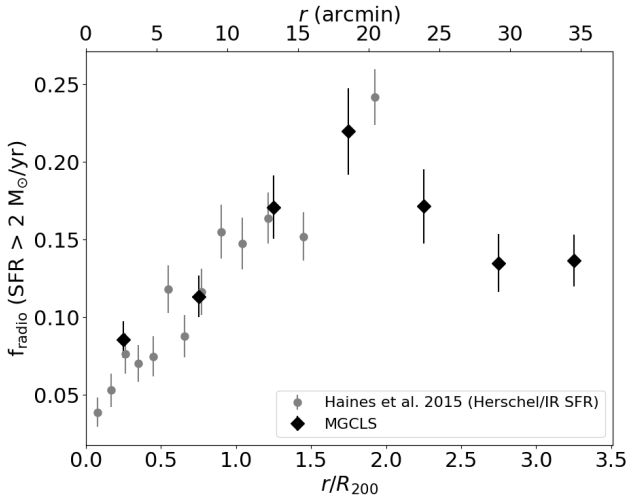

Fig. 26. Fraction of star-forming cluster members in Abell 209 detected in the radio (black diamonds) as a function of projected radial distance from the cluster centre, in units of R_{200} (bottom) and in angular units (top). We only plot MGCLS sources with SFRs greater than the 5σ detection limit of $\mathrm{SFR}_{5\sigma} = 2\,M_{\odot}\,\mathrm{yr}^{-1}$ (see Appendix B for details). Grey circles show the fraction of star-forming galaxies using infrared-derived data from Haines et al. (2015) for 30 clusters. Error bars show 1σ uncertainties. A similar trend is seen out to $2\,R_{200}$ for both the radio- and infrared-derived fractions.

The latter types are more often found in the cluster outskirts. This leads to a relation between the fraction of star-forming galaxies and the projected distance from the cluster centre (e.g. Lewis et al. 2002; Gómez et al. 2003; Haines et al. 2015).

Here we present analyses of star-formation rates (SFRs) and the radio–far-infrared (FIR) correlation for the Abell 209 cluster field as an example of the types of population studies possible with the MGCLS. We use the optically cross-matched MGCLS compact source catalogue (see Sect. 5.2.2). Abell 209, at a redshift of z = 0.206 and with R_{200} = 2.15 Mpc (10.2′ on the sky), is selected due to the availability of extensive spectroscopic catalogues from the Cluster Lensing And Supernova survey with *Hubble* (CLASH-VLT; Annunziatella et al. 2016) and the Arizona Cluster Redshift Survey[17] (ACReS; described in Haines et al. 2015) for the identification of cluster galaxies. Given MeerKAT's large primary beam, these studies can therefore be performed out to $3.5\,R_{200}$ in this cluster, unprecedented in the radio regime.

After assigning cluster membership and excising AGN (see Appendix B for details), we obtain a final catalogue of 459 MGCLS-detected star-forming cluster members within the primary-beam-corrected field of view (80 within R_{200})[18]. Figure 26 shows the fraction of star-forming cluster members that are detected by MeerKAT, $f_{\mathrm{radio}} = N_{\mathrm{MGCLS}}/N_{\mathrm{optIR}}$ (with $\mathrm{SFR} > \mathrm{SFR}_{5\sigma}$), as a function of angular distance and projected distance (in units of R_{200} = 2.15 Mpc) from the cluster centre. Here N_{optIR} is the number of cluster member galaxies determined from the optical and infrared catalogues after removing AGN contamination (2476 within the field of view). We see that the

[17] http://herschel.as.arizona.edu/acres/acres.html

[18] This catalogue forms the basis of a value-added catalogue for Abell 209 being provided with the MGCLS DR1, which includes radio-derived SFRs for each galaxy and the ratio of radio-to-FIR flux densities (where available). See Appendix B for details of these additional measurements and Table B.1 for an excerpt of the catalogue.

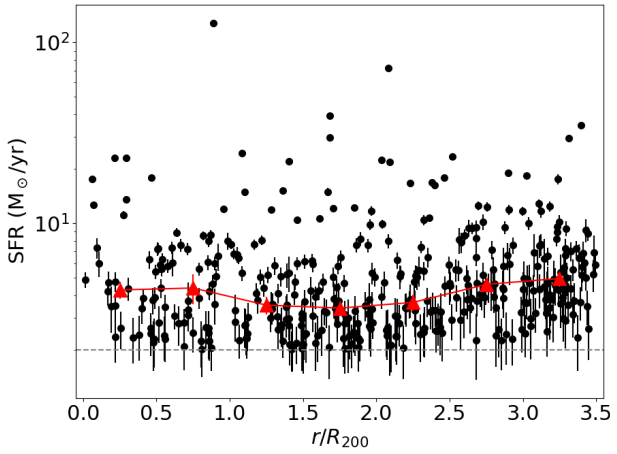

Fig. 27. SFR versus projected radial distance from the Abell 209 cluster centre, in units of R_{200}, for the 429 star-forming cluster galaxies in the full primary-beam-corrected MGCLS field of view. The red triangles indicate the median SFR plotted in radial bins and show no evolution with radial distance. The dashed grey line is the SFR at the MGCLS 5σ sensitivity limit. All error bars show the 1σ uncertainty.

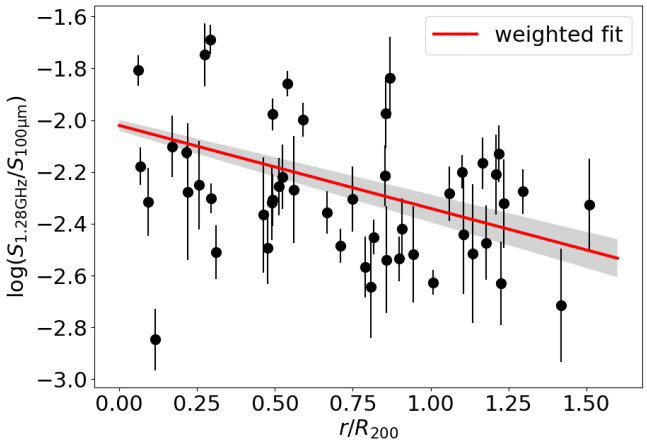

Fig. 28. Log ratio of radio-to-FIR flux densities for 49 star-forming cluster galaxies in Abell 209 as a function of projected radius from the cluster centre in units of R_{200}. Black circles indicate the star-forming galaxies in the Abell 209 cluster that have MGCLS radio and *Herschel* FIR flux densities. All error bars are 1σ uncertainties. The red line is the weighted least-squares fit given in Eq. (7), with the grey region showing the 1σ uncertainty of the fit.

fraction is lower in the cluster centre ($f_{\mathrm{radio}} < 0.1$), and rises to ~0.2 by $2\,R_{200}$. The fall in the last three radial bins is at least in part due to decreased sensitivity in the MGCLS observations due to the MeerKAT primary beam. For comparison, we show results from Haines et al. (2015) of the fraction of star-forming galaxies in a sample of 30 $0.15 < z < 0.30$ clusters, as measured using *Herschel* observations. These probe down to the same SFR limit as the MGCLS data, assume the same Chabrier (2003) initial mass function (IMF) as this work, and are not affected by dust extinction. In the region of overlap, we see a similar trend in the infrared-derived results. Haines et al. (2015) interpreted their result as evidence for relatively slow quenching of star formation in cluster galaxies over a ≈2 Gyr timescale.

8.2.1. Star-formation rates

In the last few decades there have been many efforts to measure the for galaxies in a range of environments using various tracers (e.g. James et al. 2004; Elbaz et al. 2007; Karim et al. 2011, for Hα, infrared, and radio measurements, respectively). Here we use the MGCLS radio continuum luminosities to estimate SFRs for the star-forming galaxies in Abell 209 (details of the SFR determination are provided in Appendix B). The radio signal is a combination of thermal free-free (bremsstrahlung) and non-thermal synchrotron (e.g. Condon 1992). The non-thermal emission typically dominates at frequencies below 5 GHz. The 1.28 GHz MGCLS luminosities therefore provide us with dust-unbiased measurements over a ≈1 deg^2 field centred on the cluster, probing radio-derived SFRs out to well beyond R_{200} for the first time.

Figure 27 shows the SFR of the MGCLS-detected Abell 209 star-forming member galaxies as a function of the projected distance from the cluster centre, under the assumption that the observed radio emission is due to star formation. We find no dependence of the SFR on distance from the cluster centre, based on the median SFR of the member galaxies. This is consistent with the star-formation quenching process taking place over an extended time period that is longer than the infall time (i.e. galaxies that are forming stars are not immediately quenched upon encountering the cluster environment). A similar result was found for the highest-mass star-forming galaxies in nearby clusters from the SDSS (von der Linden et al. 2010); however, the lower-mass galaxies showed more significant star-formation quenching within $0.2\,R_{200}$.

8.2.2. Radio–FIR ratio

The 1.4 GHz luminosities of star-forming galaxies are tightly correlated with their luminosities (Condon 1992), with both indicating the rate of star formation. Looking at nearby galaxy clusters ($z < 0.025$), a small but statistically significant enhancement of the radio–FIR ratio has been found for cluster galaxies as compared to the field galaxies (Reddy & Yun 2004; Murphy et al. 2009). Gavazzi et al. (1991) suggest this enhancement could be due to the ram pressure from the interaction with the ICM, which compresses the star-forming gas and amplifies the embedded magnetic fields. Using cross-matched *Herschel* 100 μm flux densities for 49 Abell 209 star-forming galaxies (see Appendix B), we examined the radio–FIR correlation, looking for evidence of evolution with distance from the cluster centre.

Figure 28 shows the ratio of radio-to-FIR flux density for Abell 209 as a function of projected distance from the cluster centre in units of R_{200}. We perform a non-linear weighted[19] least-squares fit to a straight line using the log ratio versus r/R_{200}. We obtain a best-fit relation of

$$\log\left(\frac{S_{1.28\,\mathrm{GHz}}}{S_{100\,\mu\mathrm{m}}}\right) = (-0.32 \pm 0.03)\frac{r}{R_{200}} - 2.02 \pm 0.02. \quad (7)$$

We see a statistically significant trend for the radio–FIR ratio to increase with decreasing projected distance from the cluster centre. Our results are in line with findings from Murphy et al. (2009), who argued that this primarily arises from ram pressure stripping. The amount of ram pressure is expected to be proportional to the ICM density, but should also be dependent on cluster richness and mass. The MGCLS provides a range of clusters with which to study this further, and potentially disentangle the various effects, as well as a large enough sample of

[19] Weights are the 1σ uncertainties in the log ratio.

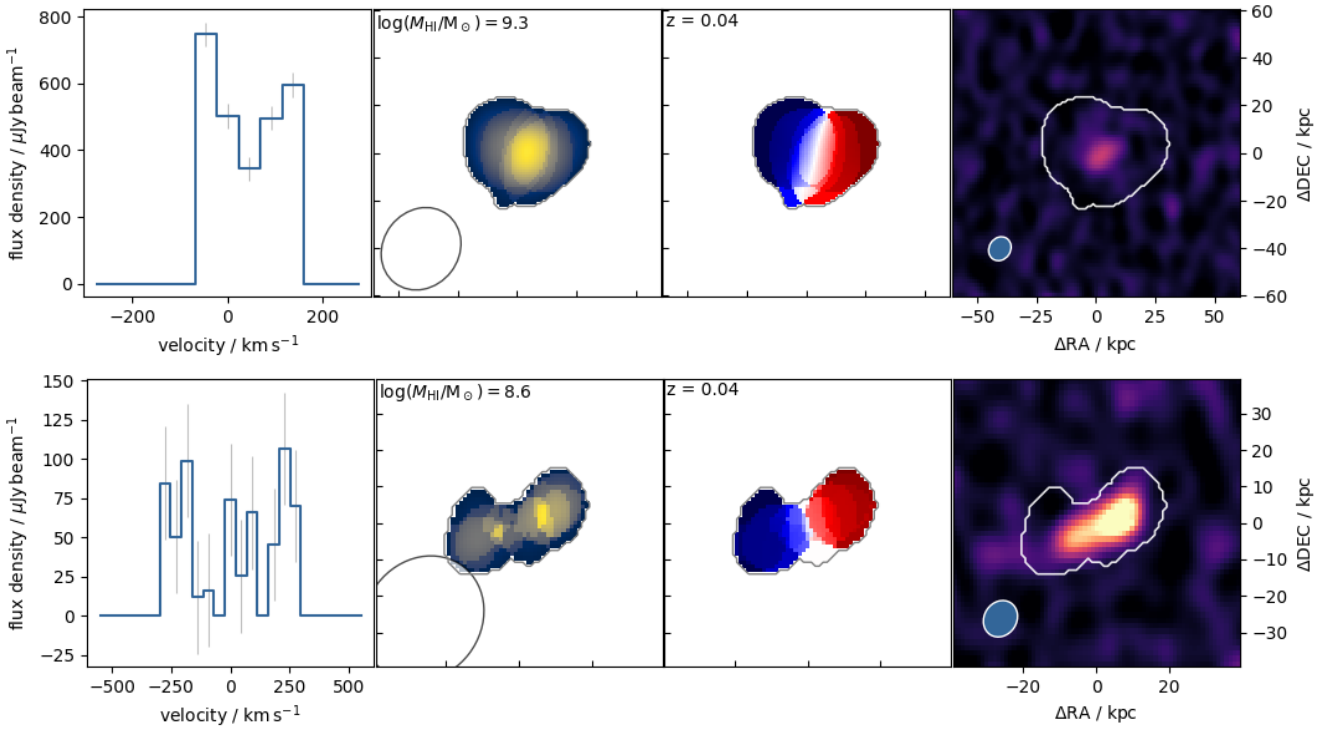

Fig. 29. Two demonstration examples of complementary H I and radio continuum science in the MGCLS from the Abell 3365 field. Both rows show H I discs at $z \sim 0.04$ with radio continuum counterparts. *Left*: integrated H I spectrum with the per-channel standard deviation indicated by grey vertical bars. *Centre left*: total intensity H I map with the synthesised beam indicated in the lower left corner. The contour outlines the lowest level emission deemed real by the SoFiA source finding software (see Sect. 9.1.2 for details). The colour scale (from yellow to blue) shows the H I flux density from the left panel. *Centre right*: H I velocity map, with the colour scale (blue to red) set to the velocities for which there is non-zero flux density in the left panel. The contour is the same as in the centre left panel. *Right*: radio continuum intensity map, with the continuum synthesised beam indicated in the lower left corner. The colour range is between −20 and 200 μJy beam^{-1}, and the contour is the same as in the centre left panel.

galaxies in individual clusters to look for dependences on galaxy properties.

9. HI science highlights

In conjunction with the continuum science discussed in previous sections, one of the great strengths of the MGCLS dataset is in its usefulness for mapping large volumes in H I (see Sect. 4.3.4). The sensitivity of the observations makes the MGCLS a rich resource for galaxy evolution studies that employ the H I line, especially in cases where there is ancillary data at other wavelengths available. Commensal H I science is possible not only within the clusters themselves, but also in the foreground and background as a result of the large H I volume probed by the long-track MGCLS observations. The H I data products themselves are not included in the current DR1.

H I MGCLS studies can make effective use of two low-RFI windows, between 1300−1420 MHz ($0 < z < 0.09$) and between 960−1190 MHz ($0.19 < z < 0.48$). While the first enables sampling of the H I mass function at lower redshifts, the second provides a glance into the most massive systems at higher redshift through statistical means and potentially by strong lensing of the clusters themselves. For cases where radio continuum and H I sources are spatially resolved, H I outflows (e.g. in starburst or AGN systems) can be studied, and comparisons can be made between the star formation and H I mass properties on both an individual and statistical basis. To demonstrate this, Fig. 29 shows two examples of H I discs in the MGCLS data, with very different radio continuum properties.

To illustrate the H I science possible with this survey we present early results from an examination of four representative galaxy clusters, selected primarily to demonstrate data quality and potential science. The clusters, Abell 194, Abell 4038, Abell 3562, and Abell 3365, lie in the redshift range $0.01 < z < 0.1$ and were selected from a heterogeneous catalogue of clusters detected in the 0.1−2.4 keV X-ray band (Piffaretti et al. 2011). They cover a reasonable range of X-ray luminosity ($L_X \approx (0.07-1.3)\times10^{44}$ erg s^{-1}) and cluster virial mass ($M_v \approx 0.4-2.4\times 10^{14}\ M_\odot$).

9.1. H I data processing

In the following two sections we describe the methodology followed to extract H I cubes for the four cluster datasets from the MGCLS visibilities, and the procedure used to carry out H I source finding.

9.1.1. H I cubes

We created H I data cubes within the frequency interval of 1305−1430 MHz ($z \lesssim 0.088$). The data reduction was conducted with the CARACAL[20] (Józsa et al. 2020) and OXKAT[21]

[20] https://caracal.readthedocs.io/en/latest/
[21] https://github.com/IanHeywood/oxkat

(Heywood 2020) pipelines. The former makes use of STIMELA[22], which is a radio interferometry scripting framework based on container technologies and Python (Offringa et al. 2010). Within this framework, various open-source radio interferometry software packages were used to perform all necessary procedures from cross calibration to imaging.

The final H I cubes of the four clusters cover a field of view of 1.0 deg^2 each, have a median rms noise level of ∼0.1 mJy beam^{-1} per 44.1 km s^{-1} channel, and a median FWHM Gaussian restoring beam of ∼18″ (imaged with natural weighting). This noise level results in a typical 5σ H I column density sensitivity of 9×10^{19} cm^{-2} (0.72 $M_\odot$ pc^{-2}) over a line width of 44.1 km s^{-1}.

9.1.2. H I source finding

We used the H I Source Finding Application (SoFiA, Serra et al. 2015) to search for line emission from each of the cubes. For this purpose, various tests were conducted with SoFiA noise threshold filters, smoothing kernels, and reliability parameters to ensure optimal source finding that reduced the number of false positives and ensured that the low H I surface brightness is also properly detected. We used the smooth and clip (S+C) method (Serra et al. 2012), with a noise threshold of 4 times the rms noise and spatial smoothing kernels corresponding to 1.0, 1.5, and 2.0 times the synthesised beam. Given the coarse 44.1 km s^{-1} velocity resolution of the MGCLS data, no smoothing was done in velocity. The catalogue of detections was compiled retaining only the positive voxels with an integrated $S/N > 3.5$ and reliability parameter >0.99. This high SoFiA reliability was chosen to limit the rate of potential false detections. All detections were additionally validated by eye.

9.2. H I science examples

Here we highlight a select few of the results from this initial set of cluster analysis. As previously emphasised, these include H I detections within the clusters themselves, as well in their foregrounds and backgrounds.

9.2.1. The distribution of H I masses

Figure 30 shows the H I mass distribution of all galaxies detected in H I in clusters Abell 194 ($z = 0.018$), Abell 4038 ($z = 0.028$), and Abell 3562 ($z = 0.049$). The H I detection cluster membership was defined within the velocity dispersion of the clusters and the entire 1 deg^2 field of view and may therefore contain interlopers. Abell 3365 ($z = 0.093$) is not included here as the frequencies corresponding to its redshift were heavily contaminated by RFI – a demonstration of the upper redshift limit of the $0 < z \lesssim 0.09$ RFI-free window.

The mass distributions in these three clusters point towards different H I populations in different clusters. The H I (redshift-dependent) mass detection limit lies below the low-mass drop in the detection rate for Abell 3562, and the lack of low-mass detections in this system is therefore not sensitivity related. By comparison, Abell 4038 shows a deficiency in high-mass H I detections. These two systems are of comparable mass (2.4×10^{14} $M_\odot$ versus 2.0×10^{14} $M_\odot$); however, Abell 3562 is part of the rich Shapley supercluster (Raychaudhury et al. 1991), and this environment may impact the H I mass in the system. Abell 194 is almost an order of magnitude less massive (4.0×10^{13} $M_\odot$), which may account for the comparatively low number of H I galaxies detected in the system.

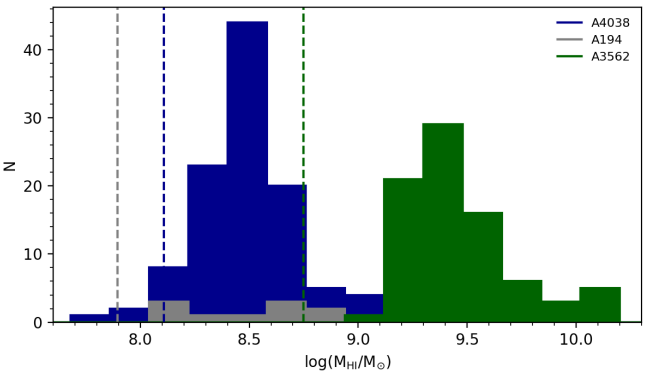

Fig. 30. HI mass distribution of detected galaxies in Abell 194, Abell 3562, and Abell 4038. Dashed vertical lines indicate the HI mass detection limits at the distances of each cluster, assuming a galaxy line width of 150 km s^{-1} detected above 4σ.

9.2.2. Cluster H I: Abell 194

In Fig. 31 we show the H I total intensity map of Abell 194 overlaid on an optical image. This shows the extent, richness, and some of the presumably environment-driven morphological transformation processes that influence the growth and evolution of these cluster members. By studying the full sample of appropriate clusters in the MGCLS sample, we will be able to investigate these effects on a statistical basis with a relatively uniform set of observations, as well as find rare extreme examples, given the large sample size.

9.2.3. Foreground H I: Discovery of a new H I group

The H I imaging of Abell 3365 was compromised by severe RFI at the frequency corresponding to $z = 0.0926$. However, this dataset showed the value of our strategy of imaging the full $0 < z \lesssim 0.1$ range through the serendipitous discovery of a massive H I group in the foreground of Abell 3365 at $z = 0.040$. This group, with a dynamical mass of $M_{\rm dyn} \sim 10^{13}$ $M_\odot$, has at least 26 members, some of which have disturbed and asymmetric H I morphologies as seen towards the centre of the group's H I moment-0 map shown in Fig. 32.

10. Summary and conclusions

We have presented a technical description and initial science results from the MGCLS DR1, which consists of 1.28 GHz observations of 115 radio- and X-ray-selected galaxy clusters. The full list of MGCLS targets and associated legacy product status is available in Table 1. We note that the clusters were not selected to be a homogeneous or complete sample, so care must be taken in any statistical investigation of our cluster sample as a whole.

The available DR1 products are composed of: visibilities; full field of view basic cubes without primary beam correction; primary-beam-corrected full-resolution (7−8″) and convolved (15″) Stokes-I intensity and spectral index cubes; and full-resolution primary-beam-corrected 12-frequency spectral cubes. For 40% of the clusters, full Stokes cubes suitable for Faraday rotation analysis, and limited-purpose single-plane Q and U

[22] https://github.com/ratt-ru/Stimela